https://doi.org/10.5194/essd-2020-242
Preprint. Discussion started: 13 October 2020

Realtime WRF LES Simulations to Support UAS Flight Planning and Operations During 2018 LAPSE-RATE

James O. Pinto, Anders A. Jensen, Pedro A. Jiménez, Tracy Hertneky, Domingo Muñoz-Esparza, Arnaud Dumont and Matthias Steiner

National Center for Atmospheric Research,

Research Applications Laboratory,

Boulder, Colorado

Corresponding author: James Pinto, pinto@ucar.edu

https://doi.org/10.5194/essd-2020-242
Preprint. Discussion started: 13 October 2020

Open Access Earth System Science Data Discussions

Abstract

The simulations were forced using data from the High-Resolution Rapid Refresh (HRRR) and the Global Forecast System (GFS) obtained from the National Center for Environmental Prediction (NCEP) Central Operations (NCO). The nested WRF configuration used in this study featured a large-eddy-permitting, 111-m grid spacing mesh for the inner-most domain. Output from the WRF forecasts were processed on-the-fly using the Unified Post Processor (UPP). A THREDDS data server was coupled with a web-viewer to provide real-time graphics that were used to support UAS flight planning and decision making. The simulations ran in under six hours on the National Center for Atmospheric Research (NCAR) Cheyenne supercomputer using 59 cores (2124 processors). The simulations were run twice per day (12 runs total during the experiment) to support both next-day mission planning and day-of tactical guidance. The simulations provided a high-resolution depiction of the four-dimensional variability of weather conditions across the northern half of the San Luis Valley, Colorado, where UAS operations took place. The simulations were used to assess the possibility of a number of small UAS weather hazards including wind shift boundaries, vertical shear, strong thermals, turbulence intensity, fog, low ceilings, and thunderstorms. Details of the model configuration used to perform the simulations and the data processing steps used to produce the final grids of state variables and other sensible weather products (e.g., ceiling and visibility, turbulence) are given. A few examples of predictive capabilities of the modeling system are provided to illustrate the skill of the model at predicting fine-scale boundary layer structures and turbulence associated with drainage winds, up-valley flows, and convective storm outflows. A subset of the at data is available at the Zenodo data archive (https://zenodo.org/communities/lapse-rate/) while full dataset (see Pinto et al. 2020a) is archived on the NCAR Digital Asset Services Hub (DASH) and may be obtained at http://doi.org/10.5065/83r2-0579.

https://doi.org/10.5194/essd-2020-242
Preprint. Discussion started: 13 October 2020

1. Background

The LAPSE-RATE field program took place in July of 2018 in the San Luis Valley (SLV) of Colorado. The goal of this project was to utilize a fleet of small UAS to sample sub-mesoscale variability occurring in the lower atmosphere of an alpine desert valley that resulted from surface-air interactions within complex terrain characterized by heterogeneous surface conditions (de Boer et al. 2020a). Several meso-gamma-scale (i.e., 2-20 km in extent) circulations were expected including drainage winds, valley flows, and thunderstorm outflows; however, the strength and depth of these flows was not well known due to a lack of observations in the area. The impact of surface heterogeneities (specifically irrigated cropland versus fallow fields and desert shrubs) on boundary layer evolution and their influence on triggering moist deep convection was also targeted with UAS missions. The performance and recoverability of small UAS can be influenced by weather conditions (gusty winds, vertical wind shear, thermals) that may be considered benign by general aviation.

As commercial uses of small UAS continue to expand, fine-scale weather information at scales much smaller than that currently resolved by operational numerical weather prediction (NWP) models will be needed to ensure safety and improve cost-effectiveness of operations (e.g., Campbell et al. 2017, Glasheen et al. 2020; Steiner 2019; Garrett-Glaser 2020). For example, Campbell et al. (2017) point out that analyses and forecasts of winds and turbulence in the lower atmosphere are currently not adequate for supporting efficient UAS Traffic Management (UTM) that require accurate wind information at scales relevant to UAS routing structures. At the same time, Roseman and Argrow (2020) note the importance of accurate high resolution depict of weather hazards and associated uncertainties in order to assess UAS flight risks under a range of atmospheric conditions, environments and population densities. The LAPSE-RATE field experiment offered an opportunity to work with UAS operators to better understand their needs and potential risks in a high alpine desert environment characterized by a range of small-scale flow patterns. At the same time, atmospheric data collected during the experiment can be used to assess value in WRF LES predictions over that currently available operationally. The LAPSE

https://doi.org/10.5194/essd-2020-242
Preprint. Discussion started: 13 October 2020

RATE data also offers the first substantial UAS deployment that can be used to assess the potential value of UAS data assimilation in relatively data sparse areas.

The process of driving a Large Eddy Simulation (LES) model with time-varying mesoscale forcing at the lateral boundaries is known as mesoscale-to-microscale (M2M) coupling (Haupt et al. 2019). The need for high-resolution environmental prediction spans many economic sectors, from producing more accurate estimates of wind energy production (Olson et al. 2019), to predictions of localized rainfall amount for hydrometeorology and enabling more granular forecast guidance for flash flooding (Silvestro et al. 2019), and to producing weather information for precision agriculture (Tesfuhuney et al. 2013). In addition, accurate wildland fire prediction requires simulating the impact of fine-scale terrain features on air flows as well as fire-weather feedbacks that occur at O(100 m) scales (Jiménez et al. 2018). In wind energy, wind farm operators need a high-resolution depiction of wind flow variations across their turbine arrays in order to estimate energy output (Liu et al. 2011). Early on, Bryan et al. (2003) demonstrated the importance of resolving fine-scale flow features in order to accurately simulate the evolution of tornado- and flash flood-producing super cell convective storms.

The grid-spacing used in operational NWP models has been rapidly decreasing over the past two decades but leveled off in recent years. At grid-spacings of less than 1 km, the partial differential equations describing the spatiotemporal evolution of weather begin to resolve circulations in the boundary layer that are treated by planetary boundary layer (PBL) schemes. At the same time, turbulence closure schemes used in LES are not designed to operate at grid resolutions greater than ~100 m. Because of these issues, Wyngaard (2004) named this problematic range of grid spacings (100 m-1 km) the “terra incognita.” Thus, simulating the impact of mesoscale flows on local turbulence properties of the atmosphere requires a substantial increase in the resolution between the mesoscale and microscale grids (e.g., Muñoz-Esparza et al. 2017).

Over the past 5 years, work has progressed on M2M coupling (Haupt et al. 2019). It has been shown that the performance of mesoscale models running at sub-kilometer grid spacing may actually be degraded. For example, Rai et al. (2016, 2019) have shown how skill of a mesoscale model forecast can actually degrade when using grid-spacings of between 0.5 to 1.25 km. These

https://doi.org/10.5194/essd-2020-242
Preprint. Discussion started: 13 October 2020

findings are important when considering that current operational forecasting centers are beginning to implement grid meshes with O(1km) grid spacing. As mentioned above, grid spacings of between 150 m and 1 km are too coarse for sub-grid-scale parameterizations used in LES to work properly, and have been shown to systematically over-estimate turbulence energy content (Doubrawa and Muñoz-Esparza, 2020). Thus, general guidelines for M2M have been developed that recommend avoiding the range of grid resolutions that span the terra incognita. Another key consideration in M2M coupling is the distance from the LES domain edge required to fully spin up turbulence motions within the LES grid. Muñoz-Esparza et al. (2014) demonstrated that in the absence of spun up turbulence leads to an imbalance between the subgrid-scale and resolved components that not only degrades turbulence estimations but that also results in spurious vertical distributions of wind speed. Markowski and Bryan (2016) have reported that LES without properly developed turbulence produces unrealistic near-surface vertical wind profiles containing excessive vertical wind shear. Muñoz-Esparza and Kosović (2018) have shown that the distance required for turbulent motions to fully develop is related to the ratio of the convective velocity scale and the horizontal mean wind during convective daytime conditions.

These considerations must be taken into account when designing a M2M forecast system. The next section (Section 2) describes the model configuration used to generate real-time microscale forecast guidance to support both the Intensive Operation Period (IOP) planning and small UAS operations during LAPSE-RATE. Examples of the guidance products that were generated during the experiment and preliminary comparisons with observational datasets are given in Section 3. A detailed description of file naming conventions and data formats is provided in Section 4, with Section 5 providing a brief summary of the dataset.

2. Model Configuration

Version 3.9.1.1 of the Weather Research and Forecasting (WRF) model (Skamarock and Klemp 2008, Skamarock et al. 2008) was configured and automated to generate twice-per-day fine-scale simulations to support UAS operations. The system was adapted from that developed by Jiménez

https://doi.org/10.5194/essd-2020-242
Preprint. Discussion started: 13 October 2020

et al. (2018) to support wildland fire management. Control scripts were developed and adapted to ingest model forcing datasets, convert them to WRF input data formats, execute a nested WRF model configuration, and post process model data to provide UAS weather hazard guidance in real time. Guidance on local winds, thermal, and turbulence patterns required implementation of a WRF LES grid (inner most mesh in Fig. 1) capable of resolving terrain-driven flows and boundary layer structures on scales relevant for UAS flight planning. The simulations were performed twice per day on the Cheyenne supercomputer (CISL 2019). The real-time predictions and post-processing were run in under 5 hours using 59 cores (2124 processors)[1]. Details of the model configuration are given in Table 1 and described further below.

A schematic representation of the run-time configuration is shown in Fig. 2. The simulations used to support next-day planning were driven at the lateral boundaries of D01 using forecast data from the 12:00 UTC run from NCEP's GFS model (version 14). A detailed description of the GFS is provided online.[2] The GFS runs at 18 km resolution and uses advanced techniques for assimilation of data collected from platforms ranging from surface met stations to satellites. For day-of planning, D01 was initialized and forced using the 04:00 UTC run of the HRRR model (version 2), also run at NCEP. In additional to hourly cycling to assimilate conventional observations, the HRRR also performs 15-min cycling to assimilate radar reflectivity data using latent heat nudging within the 3 km grid mesh using Gridpoint Statistical Interpolation (Benjamin et al. 2016) with a new 18-hour HRRR forecast issued each hour. The D01 domain is run for 6 or 16 hours depending on the forecast input (HRRR versus GFS, respectively) to allow model dynamics and thermodynamics to come into balance prior to initiating the WRF LES grid. Sensitivity studies revealed that a 6-hour spin-up period provided an adequate amount of time for noise and spurious gravity waves in D01 to dissipate, thus providing well balanced flows on the lateral boundaries of D02.

In both simulations, the innermost WRF LES domain (i.e., D02) is initialized at 10:00 UTC with simulations being integrated 12 hours out to cover the period of interest for UAS flight planning and deployment. The requirement for simulations to be available for planning purposes dictated

[1]Processor specs: 2.3-GHz Intel Xeon E5-2697V4 (Broadwell) processors, 16 flops per clock
[2]https://www.emc.ncep.noaa.gov/emc/pages/numerical_forecast_systems/gfs/implementations.php

https://doi.org/10.5194/essd-2020-242
Preprint. Discussion started: 13 October 2020

the domain configuration, domain size, grid spacing, and which operational forecast models were used to drive the M2M system. The runs were generally available at 4 pm (GFS-forced runs) and 4 am (HRRR-forced runs) MDT each day. The run available at 4 pm was used by LAPSE-RATE participants to decide which IOP flight configurations to deploy the next day. The day-of guidance, available at 4 am, was used to assess if weather situations had notably changed with specific emphasis on potential flight hazards, which were communicated to the team via emails and texts.

In order to perform simulations with M2M coupling in real time, a refinement ratio of 9:1 between the parent domain (D01, 1 km grid spacing) and the WRF LES grid (111 m grid spacing) was used. This nesting ratio is identical to that used by Muñoz-Esparza et al. (2018) and Jiménez et al. (2018) with the key goal of this large decrease in grid spacing being to minimize the impact of the terra incognita range of grid resolutions for which boundary-layer parameterizations were not designed (Wyngaard 2004, Zhou et al. 2014). Thus, turbulence is parameterized on the 1 km grid mesh using the MYNN PBL parameterization (Nakanishi and Niino 2009), whereas on the innermost mesh an attempt is made to resolve scales containing the most energetic turbulent scale motions using 111 m spacing between grid points. The turbulent kinetic energy (TKE) of the sub-grid scale motions within the LES grid were diagnosed following the treatment described by Lilly (1966, 1967) and formalized in terms of grid-spacing dependent eddy diffusivities by Deardorff (1980) in their equation 6.

While Rai et al. (2019) indicate that the MYNN scheme was prone to developing spurious structures in the PBL at horizontal resolutions comparable to the boundary layer depth, Muñoz-Esparza et al. (2017) found that, in general, the MYNN scheme performed best in simulating the evolution of the boundary layer throughout the diurnal cycle when used in models with spacings greater than 1 km. In addition, Rai et al. (2019) found that performance of the WRF LES is less sensitive to the PBL scheme used in the parent domain than it is to the sub-grid-scale turbulence parameterization used in the LES domain. A similar conclusion was found by Liu et al. (2020) in simulating flows over complex terrain. Thus, it was decided to use the MYNN scheme, since the simulations spanned the transition from stable nocturnal morning boundary layer to daytime convective boundary layer.

Finally, it should be noted that the cell perturbation technique outlined by Muñoz-Esparza et al. (2014). As it turned out, boundary layer wind flows were rather weak and localized during LAPSE-RATE; thus, PBL growth was dominated by local changes in instability which obviated the need for using perturbation strategies at the lateral boundaries, since turbulent vertical transport was dominant (Muñoz-Esparza and Kosović, 2018). In addition, the large extent of our domain ensured flow equilibration within the region of interest (far removed from the WRF LES lateral boundaries).

Surface fluxes were computed using the revised MM5 surface layer parameterization which includes updates to the Monin-Obukhov-based surface layer parameterization, improving the computation of surface layer fluxes by smoothly extending the stability function over a wide range of stability conditions following Jiménez et al. (2012). This treatment greatly improves the simulation of surface fluxes under more extreme stability conditions experienced during LAPSE-RATE. Land surface type, which determines the surface roughness length and albedo (among other properties) was prescribed using 1-km resolution MODIS 20-category data. Terrain was also prescribed using 1 km data from the U.S. Geological Survey (USGS). General properties of the model configuration and a listing of the physical parameterizations used to produce the simulations are provided in Table 1.

A stretched terrain following coordinate is used in each grid with vertical resolution of less than 150 m in the lowest 1.25 km of the model (Fig. 1). The top of the model was moved from standard height of 50 hPa to 200 hPa (i.e., omitting model levels in stratosphere) in order to accommodate increased vertical resolution required to resolve meso-gamma-scale flows and the larger coherent eddy structures within the evolving boundary layer. The influence of this reduced model top was shown to have minimal impact on the evolution of the lower atmosphere in previous simulations (Jiménez et al. 2018). Vertically-propagating gravity waves are attenuated using w-Rayleigh damping within a 5000 m deep layer below the model top with a damping coefficient of 0.2 s^{-1} (Klemp et al. 2008).

https://doi.org/10.5194/essd-2020-242
Preprint. Discussion started: 13 October 2020

The raw model data was post-processed using a modified version 3.2 of the UPP (see UPP Users Guide V3.0 for details[3]) and sent to a data server for immediate rendering as images that could be viewed within a web-based display. Modifications include computation of relative humidity, TKE and vertical velocity, expanding the number of flight levels available, and handling sub-hourly data. Images from the LES grid were used during the daily weather briefings to support next-day flight planning. The UPP was configured to immediately post-process the data from both D01 and LES domains. The UPP was used to de-stagger the u- and v-components of the wind field so that the wind and mass fields were all on a common grid. Data were also vertically interpolated from the computational sigma coordinate system to flight levels. In order to save space, only data from 20 flight levels spanning the lowest 5 km AGL of the simulations are available in the archive. These three-dimensional data grids were stored every 10 minutes. Fine temporal resolution profiles and near-surface variables were stored for select model grid points that corresponded with locations where fixed assets were deployed during LAPSE-RATE (Fig. 1). A detailed description of the file naming convention and the content of each file stored in the archive is given in Section 4.

3. Data products and preliminary assessment

An overview of model performance over the course of the LAPSE-RATE field experiment is shown in Fig. 3. The simulated 10-m winds obtained from all six simulations that were driven with HRRR input data are shown in Fig. 3. Modeled 10-m winds obtained from both domains are compared with winds measured by an Automated Weather Observing Station (AWOS) that was located at Saguache Airfield near the mouth of Saguache Canyon (see Fig. 1 for location of the Saguache Airfield AWOS called SAG). The winds observed at SAG demonstrate a clear diurnal signal each day, with drainage winds from the northwest developing each night around midnight (00:00 MDT) and typically dissipating within 2 hours after sunrise. Stronger drainage winds were observed on the 14th, 15th, and 18th of July 2018, while the weakest drainage flow was observed on the 17th. The drainage flow observed on the 19th was the only case in which the surface winds remained from the northwest throughout the proceeding evening due to enhanced

[3]https://dtcenter.org/sites/default/files/community-code/upp-users-guide-v3.pdf

https://doi.org/10.5194/essd-2020-242
Preprint. Discussion started: 13 October 2020

northwesterly flow aloft on this day. Overall, the diurnal variability was fairly well captured in both the WRF D01 and the WRF LES domains. It is noted that the onset of drainage flow always occurred prior to the 04:00 MDT initialization time of the WRF LES domain and that the WRF D01 domain captured the onset of drainage winds quite well. Both WRF D01 and WRF LES had very similar timing for the flow reversal between 08:00-10:00 MDT. Clearly the performance of WRF D01 was critical in properly initializing and forcing the drainage flow within the nested LES domain.

Differences in the modeled evolution of the drainage flow obtained within the two domains are generally small except on the 19th when the westerly component is too strong in both WRF D01 and the WRF LES. In fact, the initialized WRF LES winds are offset from those simulated in D01 due to a large amount of variability in the D01 wind field at initialization time. Nonetheless, the winds in the two domains become consistent within about 2 hours of the WRF LES initialization. The largest differences in the winds between the two domains occurred during the daytime, with several stronger wind spikes evident within the D01simulation that did not occur within D02. Further inspection revealed that these differences were associated with differences in the placement of moist convection and subsequent outflows within the two domains.

On 17 July 2018, strong outflow winds were predicted within both domains at SAG (Fig. 3). Surface observations indicate that stronger winds did develop in the afternoon in response to convective storms evident in the Pueblo NEXRAD radar (not shown). As observed, the model predicted strong winds to develop at SAG from convective storms forming over higher terrain and propagating southward into the SLV (Fig. 4). Outflow winds exceeding 10 m s^{-1} are predicted in several locations across the SLV (e.g., at SAG and emanating from the Sangre De Cristo Mountains). The outflow boundaries are accompanied by upward motion along the leading edge of the outflow boundaries. The outflows merge with thermals organized into hexagonal-like cells which are evident in areas that have yet to be disturbed by moist convection. As is clear in Fig. 4, the 17th of July was characterized by a combination of strong winds, thermals exceeding 2 m s^{-1}, precipitation, and areas of elevated turbulence (not shown), all potential hazards to UAS safety and efficiency.

https://doi.org/10.5194/essd-2020-242
Preprint. Discussion started: 13 October 2020

As mention above, drainage winds were observed at SAG before sunrise each day during LAPSE-RATE. A drainage flow IOP took place on 19 July 2018. Figure 3 indicates fairly strong (> 6 m s^{-1}) drainage winds were predicted at SAG within both D01 and D02. Comparison of the wind field obtain from the operational HRRR run with that obtained with WRF LES at 80 m AGL reveals notable differences in the scale of variability resolved by the two models (Fig. 5). Larger scale features are relatively similar between the two models. Both indicate persistent northwesterly flow at mountain top perpendicular to the San Juan Mountain range with weaker generally southerly winds throughout the SLV. Both models also indicate the presence of drainage flow from the Rio Grande Canyon during the early morning but the HRRR indicates widespread up-valley flow across much of the SLV during this time while the WRF LES indicates the presence of narrow channels of up-valley flow. In addition, WRF LES indicates the presence of several smaller-scale (meso-gamma scale) circulations / eddies within the SLV that are not evident in the HRRR. Finally, there is evidence of drainage flow emanating from Saguache Canyon in the WRF LES simulation that is much weaker and confined in the HRRR run used to force the lateral boundaries of the M2M simulation.

By 12:00 MDT, the patterns have diverged even further. The HRRR indicates that the persistent northwesterly winds near mountain tops have weakened and winds within the SLV have rotated to upslope on both sides of the SLV with very weak winds in the center of the SLV (Fig. 5). The WRF LES maintains slightly stronger mountain top winds with notably weaker and smaller-scale areas of upslope flow along the San Juan Mountains. The WRF LES simulation also depicts evidence of the convective PBL development, which results in a small scale cellular pattern of enhanced low-level winds. Thus, the WRF LES is capturing the impact of a deepening convective boundary layer that results in downward mixing of winds aloft which the PBL scheme used in the HRRR is not able to reproduce. This difference in the treatment of the boundary layer results in large differences in the simulated peak winds near the surface in several locations away from the mountains, with the WRF LES indicating values exceeding 5 m s^{-1} while the HRRR shows speeds mostly less than 2 m s^{-1}.

Drainage winds develop in response to horizontal pressure gradients that form via differential cooling of air within the canyon (and along the canyon walls) and air at the same height out over

https://doi.org/10.5194/essd-2020-242
Preprint. Discussion started: 13 October 2020

the valley. The potential temperature patterns evident in Fig. 5c reveal the cold drainage flow in Saguache Canyon resulting in sharp horizontal gradients along a terrain-following sigma level. By noon, it is clear that temperatures in the canyon have warmed faster than surround higher terrain which results in local rising of air and a reversal of flow into the canyon. The modeled evolution of the cold pool that developed at the mouth of Saguache Canyon is compared with that observed via NSSL radiosondes (Fig. 6). Most of the NSSL soundings obtained on 19 July 2018 were collected roughly 11 km southeast of Saguache Airport (2393 m MSL) with a surface elevation of 2313 m MSL. The five radiosondes that were launched indicate that the cold pool was generally less than 100 m deep with a temperature deficit of 5°C. The WRF LES captures the strength of this shallow inversion layer fairly well. The modeled strength of the surface-based inversion is also readily apparent in the modeled temperature profile shown in Fig. 1 (red shows modeled temperature profile at NSSL site). Both the modeled and observed potential temperature profiles exhibit a weakly stably stratification above the surface based inversion.

The WRF LES captures the evolution of the magnitude and depth of this shallow cold pool as well as timing of convective mixing between 08:30 and 10:00 MDT. Note that there are some discrepancies in the stability just above the surface-based inversion, with the model indicating a deeper transition layer than observed. As observed, the modeled surface-based inversion layer has much higher relative humidity than found just above the inversion layer, but the model is generally drier than observed. Both the sounding observations and model data depict the relative humidity decreasing with time near the surface in response to entrainment of drier air from above as the convective boundary layer develops.

Soundings and WRF LES data indicate significant vertical shear and temporal variability in winds within the lowest 1 km of the atmosphere. NSSL sounding data reveal that winds below 400 m are generally light and from the east-southeast prior to sunrise. This is in contrast to observations at SAG where low-level winds are from the northwest at 5 m s^{-1} at this time (Fig. 3). The 07:00 MDT sounding detects weak northwesterly flow below 100 m which indicates that drainage winds may have briefly extended to the NSSL sounding site (see Fig. 5b for location of NSSL soundings with respect to drainage flow winds obtained with WRF LES). The WRF LES data indicate the presence of much stronger and elevated drainage winds at the NSSL launch site between 05:00 and 07:15 MDT with low-level jet core winds exceeding 6 m s^{-1}. Examination of

https://doi.org/10.5194/essd-2020-242
Preprint. Discussion started: 13 October 2020

the spatial extend of the drainage flow in the WRF LES simulation indicates the presence of sharp gradients in its modeled strength and extent (Fig. 5b). Thus, small offsets in the modeled position of the drainage flow can result in significant model error when point-based comparisons are made. Evidence presented by Jensen et al. (2020) demonstrates sensitivity of the modeled drainage flow to initial conditions. They found that assimilating UAS observations generally improved the simulated evolution of the drainage flow compared to that obtained without UAS data assimilation using a 1 km grid. Despite biases in the simulated drainage flow, both the WRF LES and NSSL soundings indicate that east-southeast winds deepen with time after sunrise in response to daytime heating (Fig. 6c,d).

A key aspect of the WRF LES simulations is the ability to explicitly resolve convective boundary layer structures (Nolan et al. 2018) and meso-gamma scale flows described above. Examination of the drainage flow case indicates that the WRF LES had skill in predicting the transition from a nocturnal to convective boundary layer in complex terrain. A comparison of WRF LES vertical velocity and that obtained with a Doppler lidar is shown in Fig. 7. During the predawn and early morning hours, the flow appears weakly-turbulent in both the WRF LES data and the Doppler lidar observations. Evidence for waves in the stable flow can be seen in both datasets between 05:00 and 07:00 MDT. A comparison of the vertical velocity variance indicates that the model captures most of the energy content of the observed structures that can be resolved with 5-second data. During early morning the modeled and observed distributions of vertical velocity are peaked while in the late morning the vertical velocity transitions to a much broader and positively skewed distribution, indicating that the model generally captured the evolution of the larger eddies but underestimated the broadening of the distribution as the convective boundary layer develops.

4. Description of model dataset

Data from the real-time WRF modeling system were post-processed using a modified (to handle sub-hourly output and to add some additional diagnostic output like TKE at flight levels) Version 3 of the UPP. The UPP was used to de-stagger the mass and wind field grids onto a single common grid, rotate the wind vectors from grid-relative to earth-relative frame of reference,

https://doi.org/10.5194/essd-2020-242
Preprint. Discussion started: 13 October 2020

interpolate from computational hybrid levels to heights above ground level, and compute a number of diagnostics (Table 2). A detailed description of the UPP V3.0 is available online. The grids were output every 10 min for both domains (D01 and D02). The UPP was also used to convert the data from the raw WRF netCDF format to standard WMO Grib2 data format. Specifics describing the grid projection are given in Table 3. The wind variables have been re-gridded to be at mass variable grid points.

The file naming convention follows:

WRFPRS_YYYYMMDDhhmm_dnn.lh_lm

where

YYYYMMDD is the date the model run was initialized in UTC

hhmm is the hour and minute of the day the model run was initialize in UTC

nn = domain number (01,02 – for 04:00 UTC runs or 02,03 – for 18:00 UTC runs)

lh = forecast outlook hour

lm = forecast outlook min

valid_time = hhmm + lhlm

Additional data were output in ASCII format at three locations (i.e., Saguache, Moffat, and Leach Airfield) where observational systems (both surface-based and UAS) were located during LAPSE-RATE. The ASCII output files contain model data fields at a frequency determined by the time step used to integrate the equations of motion within that domain (D01: 6 s, D02: 0.666 s). The files are stored using the following naming convention:

XXX.dnn.ZZ.yyyymmddhh.gz

where XXX is the location name (SAG - Saguache, MOF - Moffat, LEA - Leach), nn is the domain number (02 – for 04:00 UTC runs or 03 – for 18:00 UTC runs), ZZ is the variable and yyyymmddhh is the model initialization time (UTC).

These ASCII files are formatted to provide timeseries of profiles up to 1850 m AGL (where VV = 'PH', 'QV', 'TH', 'UU', 'VV', 'WW') and timeseries of surface meteorological data, vertically-integrated quantities, and stability parameters (ZZ = 'TS'). The value and units for each ZZ variable is given in Table 4. The format of the profile timeseries files is such that after the file header row, each subsequent row (or data record) includes the forecast lead time (LT) and values of the given variable for the lowest 25 model levels. The valid time in UTC is equal to hh + LT. Details of the format of the 'TS' files, which contains 19 variables per row, are given in the README file that accompanies the dataset.

5. Data availability

An overview of all of the datasets that have been archived is given by de Boer et al. (2020b), https://zenodo.org/communities/lapse-rate/). Because of the size of the model files, in particular the 3D grids, only the timeseries ASCII data files and samples of the 3D model grids are provided on zenodo (Pinto et al. 2020b). The full set of model grids and timeseries files can be obtained from the NCAR's Digital Asset Services Hub (DASH) repository at http://doi.org/10.5065/83r2-0579. (Pinto et al. 2020a). In addition, raw model data that have not been post-processed (i.e., not destaggered, hybrid levels, and stored in WRF netCDF format) are available upon direct request.

6. Summary

Microscale real-time simulations were conducted to provide support for both next-day IOP planning and day-of UAS flight operations during LAPSE-RATE. Key components of this dataset are that they were generated using a nested configuration that enabled M2M coupling in which operational forecasts from both the GFS and the HRRR model were used to drive a nested WRF model configured to produce microscale predictions in a region of complex terrain. The data were processed on-the-fly using the UPP to store the output in operationally-compatible standard Grib2 data format. Special fields were computed to support UAS operations including cloud ceiling height, radar reflectivity (used to diagnose convective hazards), visibility and turbulence intensity. The temperature and 3D velocity field generated with the WRF LES also contained relevant information with regard to the presence and intensity of thermals, the boundary layer depth, and the presence of realistic boundary layer structures (Nolan et al. 2018).

Initial comparisons between model data and observations indicate that the model generally captured the meso-gamma scale flows that characterized the low-level wind patterns in the SLV during LAPSE-RATE. Conditions that were simulated over the course of the experiment include nocturnal terrain-driven flows, valley flows, convective boundary layer evolution, turbulence structures including hexagonal open cells, transitions from stable to convective PBL to moist deep convection and development of outflows. The wealth of observations collected by the small UAS and many ancillary platforms deployed during LAPSE-RATE will be a great asset for both evaluating fine-scale weather prediction models and assessing the value of UAS data assimilation in data sparse regions and complex terrain (e.g., Jensen et al. 2020).

Authors Contributions. Dr. Pinto lead all aspects of the deployment, data analyses and was lead author on the article. Dr. Steiner developed initial concept of deploying a finescale prediction system to LAPSE-RATE. Dr. Jiménez configured, optimized, monitored the realtime nested model configuration with guidance from Dr. Muñoz-Esparza. Dr. Jensen performed data analyses and worked on final implementation of the realtime system. Ms. Hertneky implemented extensions to the UPP and set up post-processing to convert raw WRF output files to WMO standard Grib2 data format. A. Dumont developed the data display capability. All authors contributed to manuscript edits.

The authors declare that they have no conflict of interest.

Acknowledgements. The authors would like to thank Dr. Gijs de Boer (CIRES) for his tireless work both organizing and leading the LAPSE-RATE field experiment as well as his efforts to

https://doi.org/10.5194/essd-2020-242
Preprint. Discussion started: 13 October 2020

facilitate interactions amongst LAPSE rate participants. We'd also like to thank Dr. Sean Waugh (NSSL) for providing the sounding data for initial evaluation of the real-time simulations. Sincere appreciation is also afforded to Dr. Julie Lundquist (University of Colorado) for deploying and processing data from two Doppler lidars for LAPSE-RATE and to University of Colorado students Camden Plunkett and Patrick Murphy for supporting their deployment. The NSF sponsored the research and development effort needed to support the simulations and their analysis. We would like to acknowledge high-performance computing support from Cheyenne (doi:10.5065/D6RX99HX) provided by NCAR's Computational and Information Systems Laboratory, sponsored by the National Science Foundation. NCAR is funded by the National Science Foundation. This effort was supported NSF Award # AGS-1755088. Any opinions, findings, and conclusions or recommendations expressed in this paper are those of the authors and do not necessarily reflect the views of the National Science Foundation.

7. References

Benjamin, S. G., Weygandt, S. S., Brown, J. M., Hu, M., Alexander, C. R., Smirnova, T. G., Olson, J. B., James, E. P., Dowell, D. C., Grell, G. A., Lin, H., Peckham, S. E., Smith, T. L., Moninger, W. R., and Kenyon, J. S.: A North American hourly assimilation and model forecast cycle: The Rapid Refresh, *Monthly Weather Review*, **144**, 1669–1694. https://doi.org/10.1175/MWR-D-15-0242.1, 2016.

Bryan, G.H., Wyngaard, J. C., and Fritsch, J. M.: Resolution requirements for the simulation of deep moist convection. *Mon. Wea. Rev.*, **131**, 2394–2416, doi:10.1175/1520-0493(2003)131,2394:RRFTSO.2.0.CO;2, 2003.

Campbell, S. E., Clark, D. A., and Evans, J. E.: *Preliminary Weather Information Gap Analysis for UAS Operations*. *Technical Report*, Boston, MA, MIT Lincoln Laboratory, 2017.

Computational and Information Systems Laboratory (CISL): Cheyenne: HPE/SGI ICE XA System (NCAR Community Computing), Boulder, CO, National Center for Atmospheric Research. doi:10.5065/D6RX99HX, 2019.

Deardorff, J.W.: Stratocumulus-capped mixed layers derived from a three dimensional model, *Boundary-Layer Meteorol.*, **18**, 495-527, 1980.

de Boer, G., and Coauthors: Development of community, capabilities and understanding through unmanned aircraft-based atmospheric research: The LAPSE-RATE campaign, *Bull. Amer. Meteor. Soc.*, 101, doi:10.1175/BAMS-D-19-0050.1, 2020a.

de Boer, G., and Coauthors: Data generated during the 2018 LAPSE-RATE Campaign: An introduction and overview, Submitted *Earth Sys. Sci. Data.*, doi:10.5194/essd-2020-98. 2020b.

Doubrawa, P., and Muñoz-Esparza, D.: Simulating real atmospheric boundary layers at gray-zone resolutions: How do currently available turbulence parameterizations perform?, *Atmosphere* **11(4)**, 345, 10.3390/atmos11040345, 2020.

Dudhia, J.: Numerical study of convection observed during the Winter Monsoon Experiment using a mesoscale two–dimensional model, *J. Atmos. Sci.*, **46**, 3077–3107. doi:10.1175/1520-0469(1989)046<3077:NSOCOD>2.0.CO;2, 1989.

Friedl, M. A., Sulla-Menashe, D., Tan, B., Schneider, A., Ramankutty, N., Sibley, A., and Huang, X.: MODIS Collection 5 global land cover: Algorithm refinements and characterization of new datasets, *Remote Sensing of Environment*, **114**(1), 168 10.1016/j.rse.2009.08.016–182, 2010.

Garrett-Glaser, B.: Are Low-Altitude Weather Services Ready for Drones and Air Taxis? Aviation Today, https://www.aviationtoday.com/2020/04/26/low-altitude-weather-services-ready-drones-air-taxis/, 2020.

Glasheen, K., Pinto, J., Steiner, M. and Frew, E.: Assessment of finescale local wind forecasts using small unmanned aircraft systems, *Journal of Aerospace Information Systems*, **17**(4), 182–192, doi:10.2514/1.I010747, 2020.

https://doi.org/10.5194/essd-2020-242
Preprint. Discussion started: 13 October 2020

Haupt, S. E., and Coauthors: On bridging a modeling scale gap. Mesoscale to microscale coupling for wind energy, *Bull. Amer. Meteor. Soc*., **100**, 2533-2549, doi:10.1175/BAMS-D-18-0033.1, 2019.

Hong, S.-Y., and Lim, J.-O. J.: The WRF single-moment 6-class microphysics scheme (WSM6), *J. Korean Meteor. Soc*., **42**, 129–151, 2006.

Iacono, M. J., Delamere, J. S., Mlawer, E. J., Shephard, M. W., Clough, S. A., and Collins, W. D.: Radiative forcing by long-lived greenhouse gases: Calculations with the AER radiative transfer models, *J. Geophys. Res*., **113**, D13103. doi:10.1029/2008JD009944, 2008.

Jiménez, P. A., Muñoz-Esparza, D. and Kosović, B.: A high resolution coupled fire-atmosphere forecasting system to minimize the impacts of wildland fires: Applications to the Chimney Tops II wildland event, *Atmosphere*, **9**, 197, doi:10.3390/atmos9050197, 2018.

Jiménez, P. A., Dudhia, J., Gonzalez-Rouco, J. F., Navarro, J., Montavez, J. P. and Garcia–Bustamante, E.: A revised scheme for the WRF surface layer formulation, *Mon. Wea. Rev*., **140**, 898–918. doi:10.1175/MWR-D-11-00056.1, 2012.

Jensen, A. A., Pinto, J.O., Bailey, S.C.C., Sobash, R., de Boer, G., Romine, G., Smith, S.W. and M. Steiner: The impact of assimilating unmanned aircraft system observations on complex low-level wind fields in the San Luis Valley, submitted to *Mon. Wea. Rev*., 2020.

Klemp, J. B., Dudhia, J. and Hassiotis, A. D.: An upper gravity-wave absorbing layer for NWP applications, *Monthly Weather Review* 136(10), 3987–4004, doi:10.1175/2008MWR2596.1, 2008.

Lilly, D. K.: On the application of the eddy viscosity concept in the inertial sub-range of turbulence (NCAR Tech. Rep. 123), 1966.

Lilly, D. K.: The representation of small scale turbulence in numerical simulation experiments, Paper presented at the IBM Scientific Computing Symposium on Environmental Sciences, pp. 195–210, 1967.

Liu, Y., Warner, T., Liu, Y., Vincent, C., Wu, W., Mahoney, B., Swerdlin, S., Parks, K., and Boehnert, J.: Simultaneous nested modeling from the synoptic scale to the LES scale for wind energy applications, *J. Wind Eng. Ind. Aerodyn.*, **99**(4), 308–319, 2011.

Liu, Y., Liu, Y., Muñoz-Esparza, D., Hu, F., Yan, C., and Miao, S.: Simulation of flow fields in complex terrain with WRF-LES: sensitivity assessment of different PBL treatments, *Journal of Applied Meteorology and Climatology*, 1–52, doi:10.1175/JAMC-D-19-0304.1, 2020.

Markowski, P. M., and Bryan, G. H.: LES of laminar flow in the PBL: A potential problem for convective storm simulations, *Mon. Weather Rev.*, **144**(5), 1841–1850, 2016.

Muñoz-Esparza, D., Kosović, B., Mirocha, J., and van Beeck, J.: Bridging the transition from mesoscale to microscale turbulence in numerical weather prediction models, *Boundary-Layer Meteorol.*, **153**(3), 409–440, 2014.

Muñoz-Esparza, D., Lundquist, J. K., Sauer, J. A., Kosović, B., and Linn, R. R.: Coupled mesoscale-LES modeling of a diurnal cycle during the CWEX-13 field campaign: From weather to boundary-layer eddies, *J. Adv. Model. Earth Syst.*, **9**, 1572–1594, doi:10.1002/2017MS000960, 2017.

Muñoz-Esparza, D., and Kosović, B.: Generation of inflow turbulence in large-eddy simulations of non-neutral atmospheric boundary layers with the cell perturbation method, *Monthly Weather Review*, **146(6)**, 1889–1909, 2018.

Muñoz-Esparza, D., Sharman, R., Sauer, J., and Kosović, B.: Toward low-level turbulence forecasting at eddy-resolving scales, *Geophysical Research Letters*, **45**, 8655–8664, doi:10.1029/2018GL078642, 2018.

Nakanishi, M., and Niino, H.: Development of an improved turbulence closure model for the atmospheric boundary layer, *J. Meteor. Soc. Japan*, **87**, 895–912, doi:10.2151/jmsj.87.895, 2009.

Nolan, P.J., and Coauthors, Coordinated Unmanned Aircraft System (UAS) and ground-based weather measurements to predict Lagrangian Coherent Structures (LCSs), *Sensors*, **18**, 4448; doi:10.3390/s18124448, 2018.

Olson, J. B., and Coauthors: Improving wind energy forecasting through numerical weather prediction model development, *Bull. Amer. Meteor. Soc.*, 100, 2201-2220, doi:10.1175/BAMS-D-18-0040.1, 2019

Pinto, J. O., Jimenez, P. A., Hertneky, T. J., Jensen, A. A., Munoz-Esparza, D., Steiner, M.: WRF Large-Eddy Simulation Data from Realtime Runs Used to Support UAS Operations during LAPSE-RATE. UCAR/NCAR - DASH Repository [Data set], doi:10.5065/83r2-0579, 2020a.

Pinto, J. O., Jimenez, P. A., Jensen, A. A., Hertneky, T. J., Munoz-Esparza, D., and Steiner, M.: Realtime WRF Large-Eddy Simulation Data (Version V1) [Data set], doi:10.5065/83r2-0579, 2020b.

Rai, R. K., Berg, L. K., Kosović, B., Mirocha, J. D., Pekour, M. S., and Shaw, W. J.: Comparison of measured and numerically simulated turbulence statistics in a convective boundary layer over complex terrain, *Boundary-Layer Meteorol.*, **163**, 69–89, 2016.

Rai, R. K., Berg, L. K., Kosović, B., Haupt, S. E., Mirocha, J. D., Ennis, B., and Draxl, C.: Evaluation of the impact of horizontal grid spacing in terra incognita on coupled mesoscale–microscale simulations using the WRF framework, *Mon. Wea. Rev.*, **147**, 1007–1027, doi:10.1175/MWR-D-18-0282.1, 2019.

Roseman, C. A., and Argrow, B. M.: Weather Hazard Risk Quantification for SUAS Safety Risk Management, *J. Atmos. and Oceanic Tech.*, 37(7), 1251–68, doi:10.1175/JTECH-D-20-0009.1, 2020.

Silvestro, F., Rossi, L., Campo, L., Parodi, A., Fiori, E., Rudari, R., and Ferraris, L.: Impact-based flash-flood forecasting system: Sensitivity to high resolution numerical weather prediction systems and soil moisture, *J. of Hydrology*, 572, 388–402, 2019.

Skamarock, W. C., and Klemp, J.B.: A time-split non-hydrostatic atmospheric model for weather research and forecasting applications, *J. Computational Physics*, **227**, 3465–3485. doi:10.1016/j.jcp.2007.01.037, 2008.

Skamarock,W. C., Klemp, J. B., Dudhia, J., Gill, D. O., Barker, D. M., Duda, M. G., Huang, X.-Y.,Wang, W., and Powers, J. G.: A description of the advanced research WRF Version 3, National Center for Atmospheric Research, NCAR, Boulder, CO, TN-475+STR, 2008.

Steiner, M.: Urban Air Mobility: Opportunities for the weather community, *Bulletin of the American Meteorological Society*, **100**(11), 2131–2133, doi:10.1175/BAMS-D-19-0148.1, 2019.

Tesfuhuney, W., Walker, S., van Rensburg, L., and Everson, C.: Water vapor, temperature and wind profiles within maize canopy under in-field rainwater harvesting with wide and narrow runoff strips, *Atmosphere*, **4 (4)**, 428–444, doi:10.3390/atmos4040428, 2013.

Tewari, M., Chen, F., Wang, W., Dudhia, J., LeMone, M. A., Mitchell, K., Ek, M., Gayno, G., Wegiel, J., and Cuenca, R. H.: Implementation and verification of the unified NOAH land surface model in the WRF model, *20th conference on weather analysis and forecasting/16th conference on numerical weather prediction*, pp. 11–15, 2004.

Wyngaard, J. C.: Toward numerical modeling in the "terra incognita." *J. Atmos. Sci.*, **61**, 1816 – 1826, doi:10.1175/15200469(2004)061<1816:TNMITT>2.0.CO;2, 2004.

https://doi.org/10.5194/essd-2020-242
Preprint. Discussion started: 13 October 2020

Zhou, B., Simon, J. S., and Chow, F. K.: The convective boundary layer in the terra incognita, *Journal of the Atmospheric Sciences*, **71**, 2545–2563. doi:10.1175/JAS-D-13-0356.1, 2014.

https://doi.org/10.5194/essd-2020-242
Preprint. Discussion started: 13 October 2020

Table 1. Model Configuration.

Parameter	**Domain 1**	**Domain 2**	**Reference**
time step	6 s	0.667 s	
grid spacing	1 km	0.111 km	
E-W size	487	1008 (112 km)	Number of grid points (km)
N-S size	637	972 (108 km)	Number of grid points (km)
microphysics	WSM6	WSM6	Hong and Lim (2006)
longwave radiation	Dudhia	Dudhia	Dudia (1989)
shortwave radiation	RRTMG	RRTMG	Iacono et al. (2008)
radiation time step	10 min	5 min	
surface layer	Revised MM5	Revised MM5	Jiménez et al. (2012)
Land surface model	Unified Noah LSM	Unified Noah LSM	Tewari et al. (2004)
Land use	MODIS 20 category	MODIS 20 category	Friedl et al. (2010)
PBL physics	MYNN	explicit	Nakanishi and Niino (2009)
cumulus physics	none	none	

https://doi.org/10.5194/essd-2020-242
Preprint. Discussion started: 13 October 2020

Table 2. Description of gridded output variables in Grib2 format.

Field Name	Description	Levels$	Units	Notes
ELON, NLAT	Longitude, Latitude	---	deg	Lambert Conformal
UGRD, VGRD	Earth relative wind components	1,103	m s^{-1}	Converted from grid relative reference plane. Includes value at 10 m
TMP	Temperature	1,103	C	Includes value at 2 m
RH	Relative Humidity	103	%	Includes value at 2 m
DZDT	Vertical Velocity	103	m s^{-1}	Profile levels only
DZDT	Layer Mean Vertical Velocity	200	m s^{-1}	Average between sigma levels 0.8 and 0.5
MAXUVV	Maximum Downward Vertical Velocity	100	m s^{-1}	Max in previous 10 min lowest 400 hPa
MAXDVV	Maximum Upward Vertical Velocity	100	m s^{-1}	Max in previous 10 min lowest 400 hPa
PRES	Pressure	1,103	Pa	Includes value at 2 m
TKE	Subgrid-scale Turbulent Kinetic Energy	103	m^2 s^{-2}	Profile levels only
SPFH	Specific Humidity	1,103	kg kg^{-1}	Surface and 2m only.
WIND	Maximum wind speed	103	m s^{-1}	Max wind speed at 10 m in previous 10 min
APCP	Total accumulated precipitation	1	kg m^{-2} (mm)	Total accumulation up to forecast lead time.
PRATE	Precipitation Rate	1	kg m^{-2} s^{-1} (mm s^{-1})	Instantaneous
REFC	Composite Reflectivity	200	dBZ	Max in column
ULWR	Upward longwave radiative flux	1	W m^{-2}	At surface
DLWR	Downward longwave radiative flux	1	W m^{-2}	At surface
DSWR	Downward shortwave radiative flux	1	W m^{-2}	At surface
SHTFL	Sensible heat flux	1	W m^{-2}	At surface
LHTFL	Latent heat flux	1	W m^{-2}	At surface

https://doi.org/10.5194/essd-2020-242
Preprint. Discussion started: 13 October 2020

GFLUX	Ground heat flux	1	W m^{-2}	At surface
TCOLW	Total Column Condensed Water	200	kg m^{-2} (mm)	Vertically-integrated condensed water amount
PWAT	Precipitable Water (vapor only)	200	kg m^{-2} (mm)	Vertically-integrated amount of water vapor
HGT	Ceiling	215	m ASL	Height of lowest cloud base.
HGT	Terrain Height	1	m ASL	
VIS	Visibility	3	m	Note: Recommend using only data with level label of 3.
CAPE	Surface-based Convective Available Potential Energy	1	J kg^{-1}	
CIN	Convective Inhibition	1	J kg^{-1}	

$^{\$}$Level codes: 1 = surface, 3 = visibility at surface, 100= lowest 400 hPA, 103 = profile (height AGL), 200 = column, 215 = cloud ceiling height

Table 3. Projection information for Grib2 files.

Projection Property	**Values**	
Type	Lambert Conformal	
Min Lat, Lon	37.5507	-106.672
Lower-left minx, miny	-45.4529 km	-27.449654 km
Δx, N_x	1008	0.111 km
Δy, N_y	882	0.111 km
Origin Lat, Lon	37.8	-106.15

https://doi.org/10.5194/essd-2020-242
Preprint. Discussion started: 13 October 2020

Table 4. Description of variables stored for point locations in ASCII format.

Field Name	Description	Units	Notes
TS	Time series of 14 variables.	NA	See README file included with distribution.
UU	u-component of the wind	m s^{-1}	Positive is from the west
VV	v-component of the wind	m s^{-1}	Positive is from the south
WW	Vertical Velocity	m s^{-1}	Positive is upward
TH	Potential temperature	K	
PH	Geopotential Height	m ASL	
QV	Water vapor mixing ratio	g g^{-1}	
TK	Resolved Turbulent Kinetic Energy	m^2 s^{-2}	D02 only
EP	Epsilon Eddy Dissipation	$m^{2/3}$ s^{-1}	D02: Sub-grid scale EDR
TP	PBL scheme TKE	m^2 s^{-2}	D01 only
EL	PBL mixing length	m	D01 only

https://doi.org/10.5194/essd-2020-242
Preprint. Discussion started: 13 October 2020

Earth System Science Data Discussions
Open Access

Figure 1. Model terrain for D01 (1 km grid spacing) and D02 (111 m grid spacing) and land use specification for D02 obtained from MODIS 20-catergory dataset. Note that D01 was nested within a mesh with 9 km grid spacing when GFS forcing data was used. The '*', '#' and '^" mark the location of and AWOS station at Saguache Airfield (SAG), Moffat Observing Site (MOF), and Leach Airfield locations, respectively, for which high rate model output data are available. The filled circle marks the location of the NSSL soundings. WRF-LES profiles of temperature are given for three grid points (closest to SAG (black), NSSL (red), MOF (green)) for the drainage flow case valid at 06:00 MDT on 19 July 2018. The heights of the half-levels at each location are indicated by the filled circles.

Figure 2. Input, timing and availability for WRF LES simulations which were executed twice per day. Next day planning guidance was generate using forcing from the 12:00 UTC GFS run while day of guidance was driven using data from the 04:00 UTC HRRR run. Note that the GFS runs required three concentric nests to downscale from 0.25 degrees to 111 m grid spacing using in WRF LES. The dashed black line represents spin up period for D00 before D01 is initiated starting at 18:00 UTC. The red solid lines indicate the spin-up period for D01 (1 km grid spacing) in both simulations while the solid blue lines indicate the period over which WRF-LES (D02) was valid. Data and images from the next-day GFS-forced run was available at 4 pm while data and images from the day-of HRRR-forced run was available 4 am local time to support UAS flight planning.

Figure 3. Comparison of predicted u,v, and wind speed at 10 m AGL obtained from WRF D01 and WRF LES forced with 04:00 UTC HRRR with observations (OBS) obtained from an AWOS surface meteorological station at Saguache Airfield located at the base of Saguache Canyon. WRF-D01 data are instantaneous values while WRF-LES data are 10 min averages. AWOS data from SAG are plotted when available (roughly every 15 min). Night time conditions are indicated by the blue regions. Day of year is indicated along the top. The location of the SAG AWOS station is marked with an '*' in Figure 1.

https://doi.org/10.5194/essd-2020-242
Preprint. Discussion started: 13 October 2020

Figure 4. Simulated (a) 80-m winds (direction and magnitude) and 1 hour precipitation accumulation (R, color contours) and (b) vertical velocities (w) at 180 m AGL from WRF LES valid at 14:30 MDT on 17 July 2018. Region shown in (b) is a 40 km box outlined in (a) which is centered on SAG Airport. Black terrain contours are also given for reference in both panels.

Figure 5. Wind speed and direction at 80 m AGL from (a) HRRR (issued at 22:00 MDT on previous day) and (b) WRF LES and c) WRF LES potential temperature for zoomed in region denoted by the white box in (b) for forecasts valid at 06:00 MDT and 12:00 MDT on 19 July 2018. Model terrain heights are denoted by black contours. Symbols denote locations as follows: (asterisk – Saguache, star – Del Norte, filled circle – NSSL sounding site).

Figure 6. Time-height plot depicting WRF LES modeled evolution of the boundary layer during drainage flow case observed on 19 July 2018 as evident in a) potential temperature, b) relative humidity, c) wind speed and d) wind direction. NSSL sounding data (location marked with black dot in Figure 1) is overlaid within vertical columns corresponding with radiosonde launch times. Model data (with 10 min output frequency) is from inner most grid at grid point closest to 38.05° N, 160.05° W. The location of the NSSL soundings is shown in Figure 1.

Figure 7. Time height plots showing a) vertical velocity and b) sub-grid-scale TKE from WRF LES, c) observed vertical velocity from the University of Colorado Doppler Lidar and d) comparison of distributions of vertical velocity from Doppler Lidar (black) and WRF LES (red) at Saguache Airfield using 10 sec data. Red boxes in (a) and (c) indicate data used to generate histograms in (d).

https://doi.org/10.5194/essd-2020-242
Preprint. Discussion started: 13 October 2020

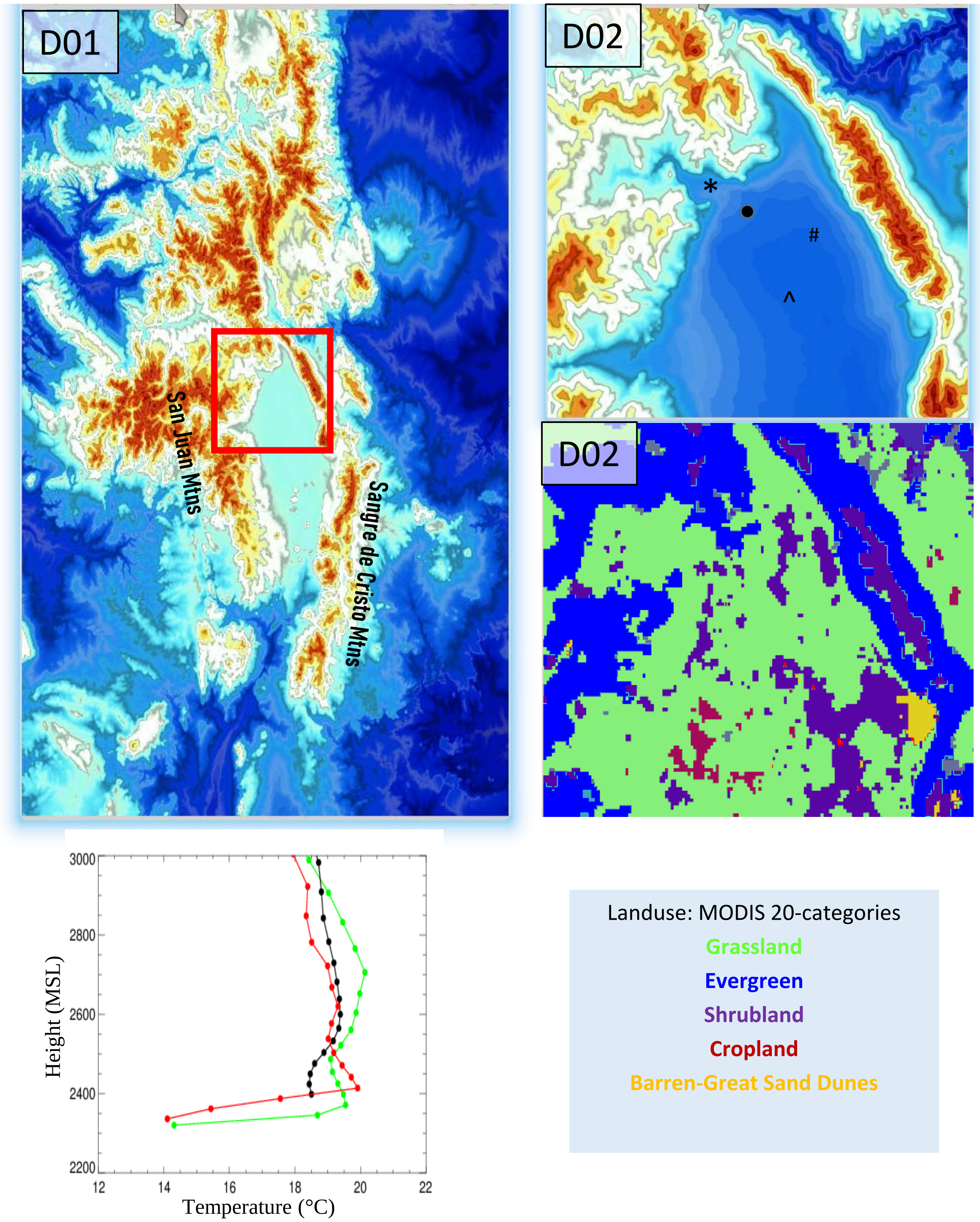

Figure 1.

https://doi.org/10.5194/essd-2020-242
Preprint. Discussion started: 13 October 2020

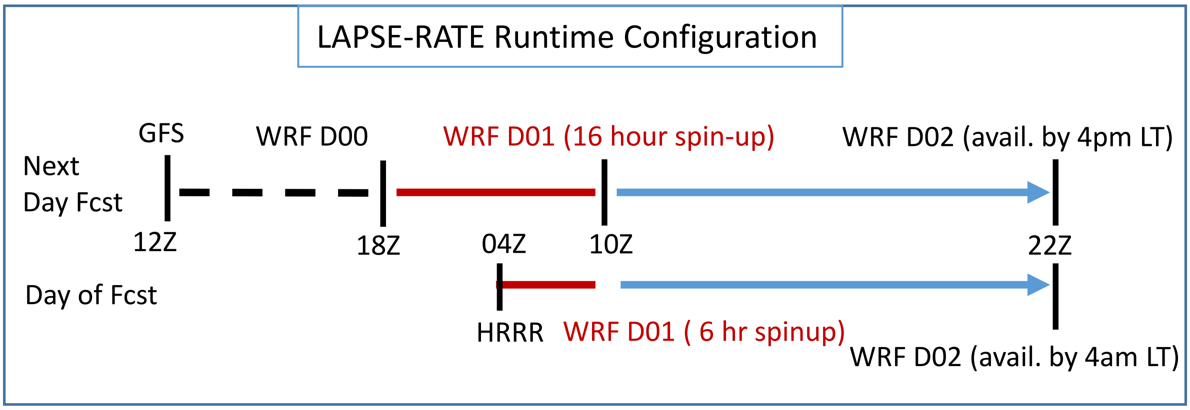

Figure 2.

https://doi.org/10.5194/essd-2020-242
Preprint. Discussion started: 13 October 2020

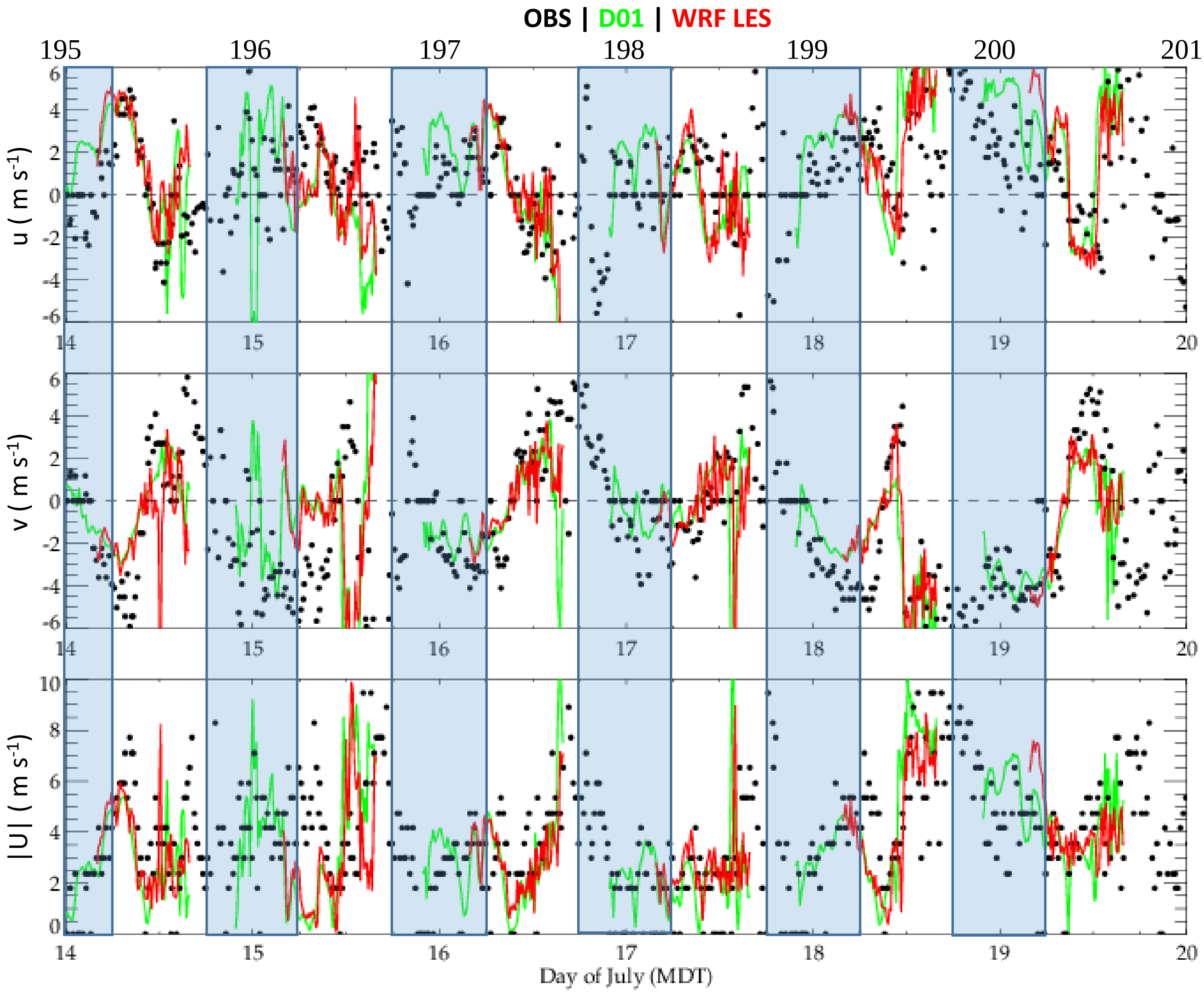

Figure 3.

https://doi.org/10.5194/essd-2020-242
Preprint. Discussion started: 13 October 2020

Open Access Earth System Science Data Discussions

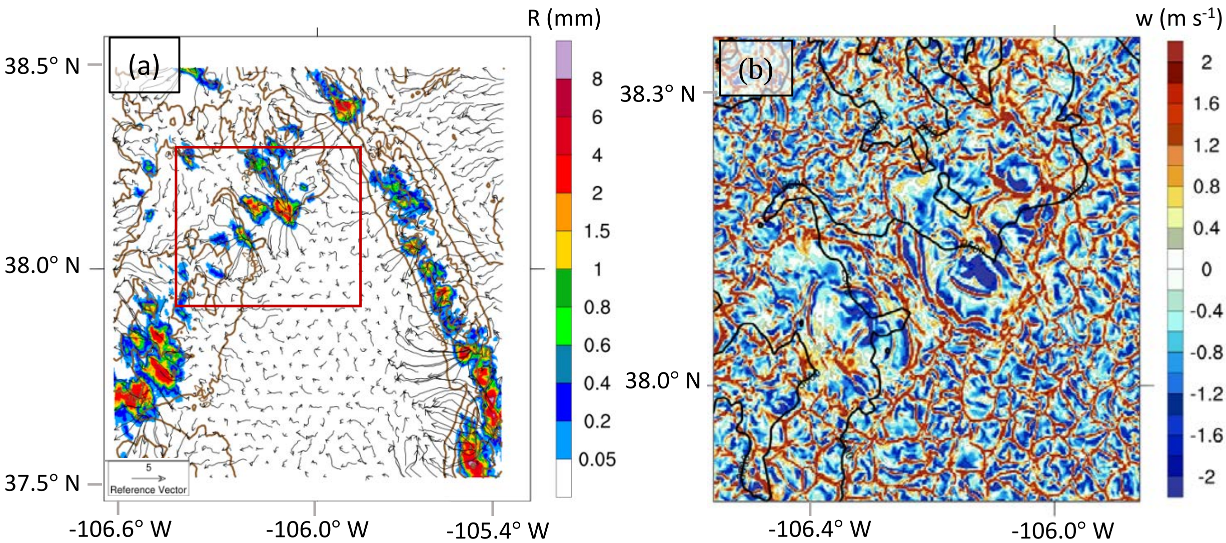

Figure 4.

https://doi.org/10.5194/essd-2020-242
Preprint. Discussion started: 13 October 2020

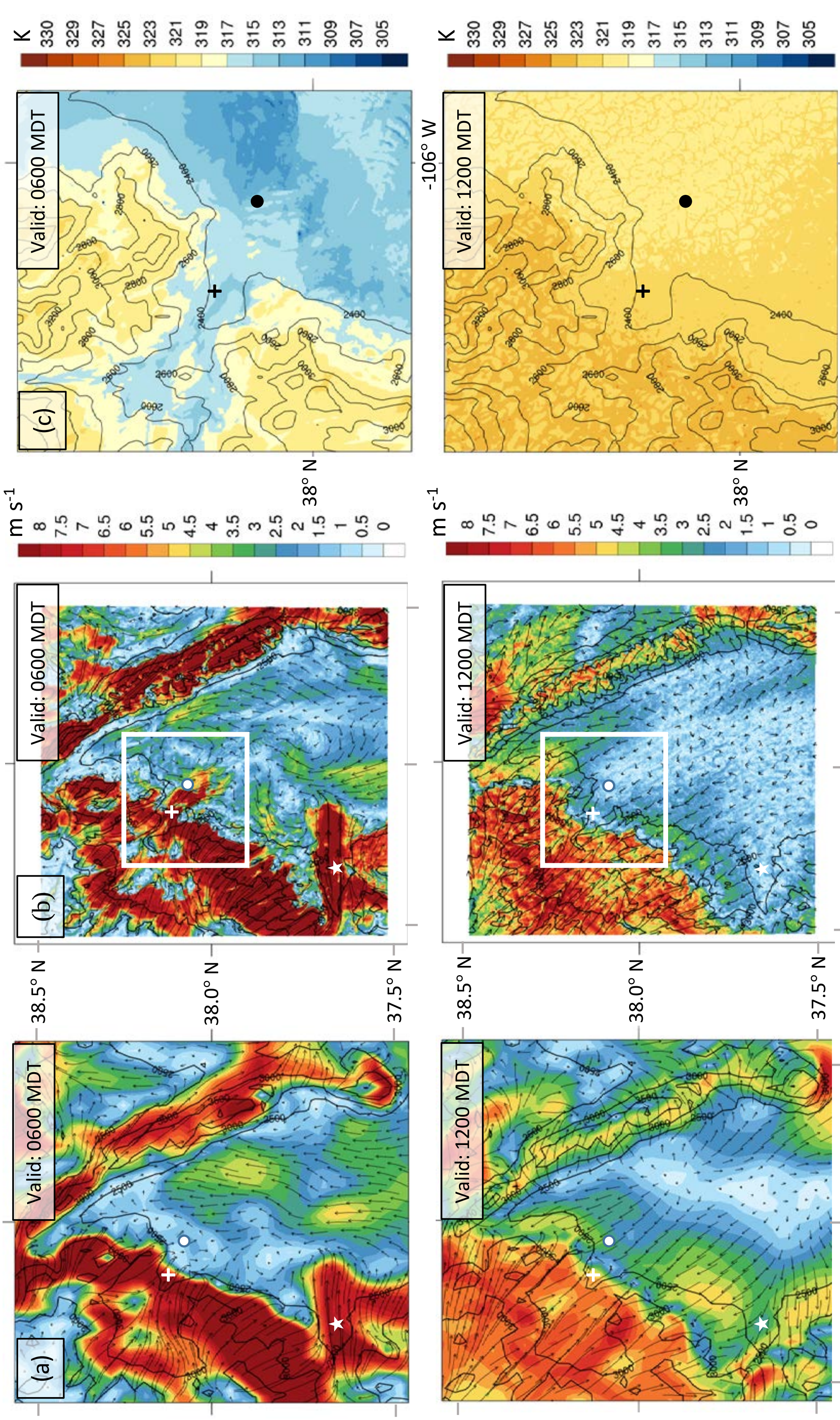

Figure 5.

https://doi.org/10.5194/essd-2020-242
Preprint. Discussion started: 13 October 2020

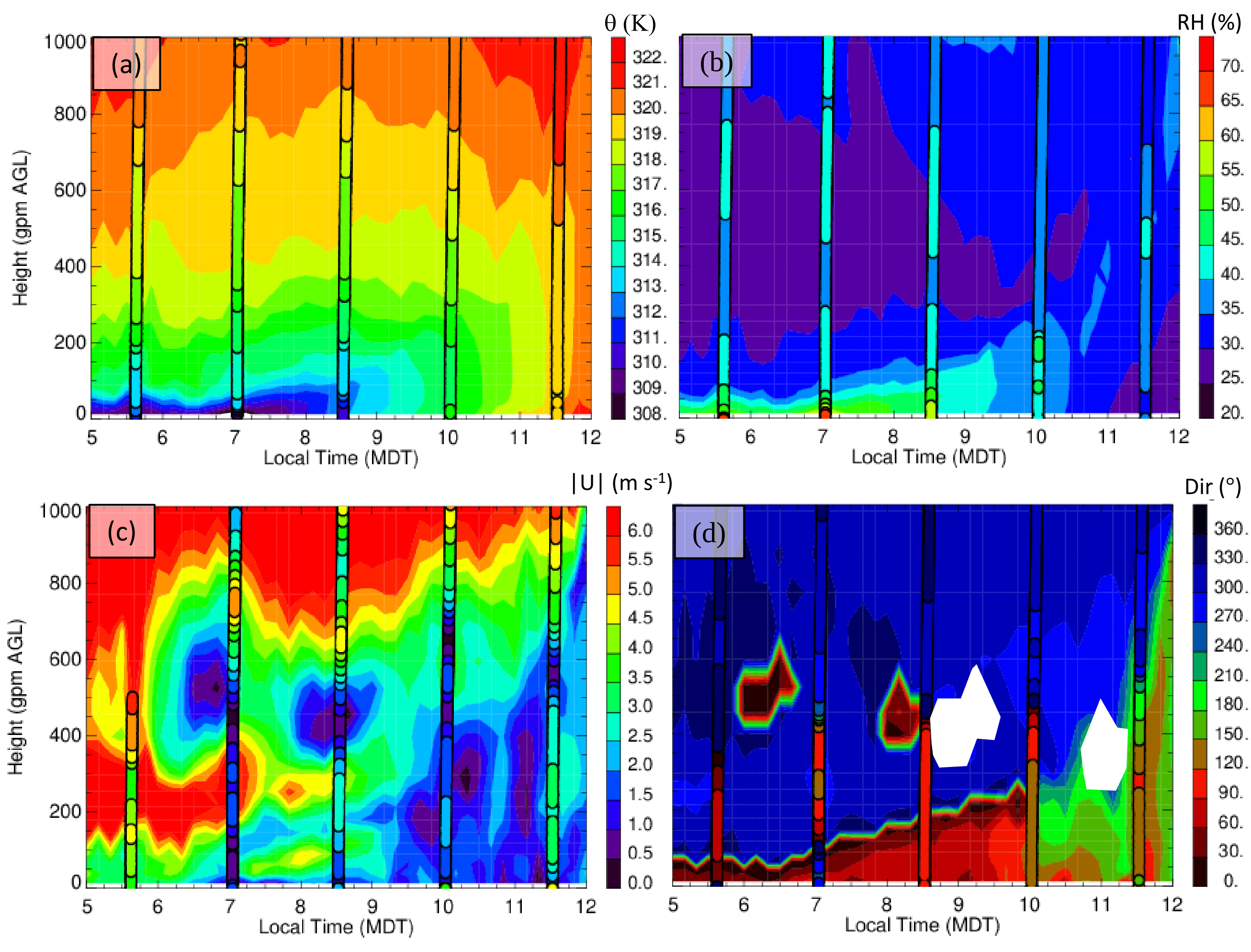

Figure 6.

https://doi.org/10.5194/essd-2020-242
Preprint. Discussion started: 13 October 2020

Open Access Earth System Science Data Discussions

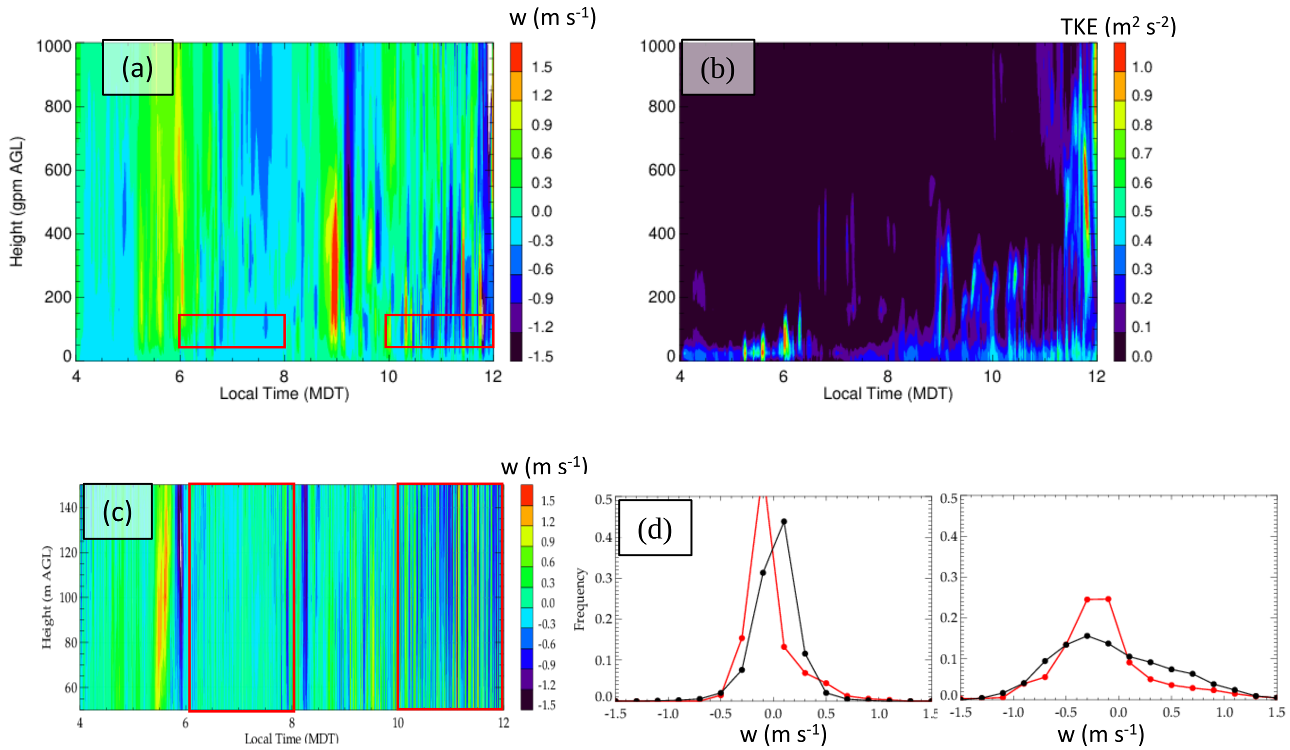

Figure 7.